Thermophysical Properties of Liquid Aluminum

MATTHIAS LEITNER, THOMAS LEITNER, ALEXANDER SCHMON, KIRMANJ AZIZ, and GERNOT POTTLACHER

Ohmic pulse-heating with sub-microsecond time resolution is used to obtain thermophysical properties for aluminum in the liquid phase. Measurement of current through the sample, voltage drop across the sample, surface radiation, and volume expansion allow the calculation of specific heat capacity and the temperature dependencies of electrical resistivity, enthalpy, and density of the sample at melting and in the liquid phase. Thermal conductivity and thermal diffusivity as a function of temperature are estimated from resistivity data using the Wiedemann–Franz law. Data for liquid aluminum obtained by pulse-heating are quite rare because of the low melting temperature of aluminum with 933.47 K (660.32 °C), as the fast operating pyrometers used for the pulse-heating technique with rise times of about 100 ns generally might not be able to resolve the melting plateau of aluminum because they are not sensitive enough for such low temperature ranges. To overcome this obstacle, we constructed a new, fast pyrometer sensitive in this temperature region. Electromagnetic levitation, as the second experimental approach used, delivers data for surface tension (this quantity is not available by means of the pulse-heating technique) and for density of aluminum as a function of temperature. Data obtained will be extensively compared to existing literature data.

I. INTRODUCTION

ALUMINUM is a silvery-whitish light metal. It is the third most common element occurring in the crust of the earth. The world aluminum statistics reports, for March 2016, the production of 4856 metric tons of aluminum worldwide. Aluminum is used in all kinds of industries, ranging from cans for drinks and foils to wrap food, to the building industry for roofing and windows, to the automotive and aerospace industries, where it is used for lightweight structures.

In production, aluminum is first melted and then undergoes different forming processes, such as casting, pressure die casting, and continuous casting. In current industrial practice, computer-based simulations allow modeling of casting, melting and remelting processes, heat transport, solidification shrinkage, residual stress, heat treatment, welding, forging, rolling, and cutting, or even predictions of microstructures. A key limitation to the successful introduction of these models is the lack of thermophysical data. Thus, experimentally obtained thermophysical properties of pure metals are of great importance as input parameters for various simulation tools and will lead to a better scientific understanding of

liquid metals and alloys as well as help in the final production to reduce waste.

Within this article, we will present a full set of experimentally obtained thermophysical properties of solid and liquid aluminum that can be used as input parameters for numerical simulations. The data presented are extensively compared to existing literature values and the range of experimental uncertainty is given for each property.

II. EXPERIMENTAL PROCEDURE AND DATA REDUCTION

A. Ohmic Pulse-Heating Experiments

High-purity aluminum wires (99.999 at. pct) with a diameter of 0.5 mm (Catalogue No. AL501115, Advent) were investigated using an ohmic pulse-heating technique. The details of the experimental pulse-heating setup have already been described extensively in References 1 through 3.

The samples with about 60 mm length were treated with abrasive paper (grade 1200), cleaned with acetone, and subsequently resistively heated under N_2 atmosphere at a pressure of 2.3 bar, starting at room temperature. A current pulse peaking at about 10 kA was discharged through the specimens and measured using an inductive coil (Model Number 3025, Pearson Electronics). At the same time, the voltage drop against common ground was measured using two Mo-foil voltage knives attached horizontally to the wire with subsequent voltage division. Due to the high heating rates of about 2×10^8 K s^{-1} needed to avoid a loss of

MATTHIAS LEITNER, THOMAS LEITNER, and GERNOT POTTLACHER are with the Institute of Experimental Physics, Graz University of Technology, NAWI Graz, Petersgasse 16, 8010, Graz, Austria. Contact e-mail: pottlacher@tugraz.at ALEXANDER SCHMON is with the Patent Attorney Dipl.-Ing. Dr. Gernot Wirnsberger, Leoben, Austria. KIRMANJ AZIZ is with the EPCOS OHG a TDK Group Company, Deutschlandsberg, Austria.

contact, the experiments had a relatively short duration of about 35 μs.

To relate the time-resolved voltage drop and current behavior to a temperature, the surface radiance was simultaneously monitored by a Peltier-cooled IR pyrometer operating at a mean effective wavelength of λ_{eff} = 2315 nm with approximately 390 nm effective bandwidth. In order to *in-situ* calibrate the pyrometer, the surface radiance at the melting plateau, observed in the radiance-over-time development, was assigned to the melting temperature of Al, *i.e.*, T_{m} = 933.47 K (660.32 °C).[4] Expressing the measured pyrometer signals by Planck's law of radiation, the surface radiance $J(T)$ measured at any time t can then be related to the observed radiance $J(T_{\text{m}})$ at the melting point by simply taking the ratio and solving for T:

$$T = \frac{c_2}{\lambda_{\text{eff}} \cdot \ln\left(\frac{J(T_{\text{m}})}{J(T)} \cdot \frac{\varepsilon(\lambda_{\text{eff}}, T)}{\varepsilon(\lambda_{\text{eff}}, T_{\text{m}})} \cdot \left\{ e^{\frac{c_2}{\lambda_{\text{eff}} \cdot T_m}} - 1 \right\} + 1 \right)}, \quad [1]$$

where c_2 = 0.014388 m K is the second radiation constant. Due to the lack of spectral emissivity data at the extreme measuring wavelength, it was further assumed that the emissivity ε takes the value that is true at the melting point, *i.e.*, $\frac{\varepsilon(\lambda_{\text{eff}}, T)}{\varepsilon(\lambda_{\text{eff}}, T_{\text{m}})} = 1$, over the entire temperature range. Note that the assumption of constant emissivity is mostly feasible in the liquid phase, while this is usually not the case for the solid phase. The data presented in this publication thus focus on the liquid phase, while the solid phase data are also given as an overall estimate.

To obtain data for the density $D(T)$, an adapted fast CCD system taking shadowgraph images of the backlit expanding wire was used (details in Reference 5). The shadow images with an exposure time of 600 ns were captured about 5 μs apart. The diameter $d(T)$ as a function of temperature can then be obtained by evaluating the full-width-at-half-maximum in the calculated intensity profile of each image. By relating this temperature-dependent diameter to the diameter d_0 imaged before the experiment, the density can be derived using a room-temperature value of D_0 = 2.70 × 10³ kg m⁻³.[6] The constraint $\frac{d_0}{d[298 \text{ K}(25 \text{ °C})]} = 1$ and, therefore, D[298 K (25 °C)] = D_0 was applied for the solid phase data fitting.

$$D(T) = D_0 \cdot \left(\frac{d_0}{d(T)}\right)^2. \quad [2]$$

Note that using this approach, longitudinal expansion must be inhibited to a high degree. This is ensured by applying high heating rates, which have shown to result in an increased radial thermal expansion at the cost of absent longitudinal expansion.[7,8] Furthermore, it is crucial to achieve a nonmoving vertical liquid metal column in order to deduce precise diameters from the intensity profiles. Therefore, density measurements were conducted as separate experiments without voltage knives that can push the metal column. In addition, the wire length was shortened to about 40 mm to increase its stability.[8]

For nondensity experiments conducted with the pulse-heating apparatus, the electrical resistivity and the specific enthalpy can be derived. From the measured time-dependent voltage drop $U(t)$ across the investigated length l, the time-dependent current $I(t)$, and the diameter at room temperature d_0 (measured with a Keyence LS-7010 laser micrometer), the specific resistivity at initial geometry (IG) is obtained as

$$\rho_{\text{IG}}(t) = \frac{U(t)}{I(t)} \cdot \frac{d_0^2 \pi}{4 \cdot l}. \quad [3]$$

In order to correct for thermal volume expansion (VE), the radial expansion data obtained for density measurements are used. The correction is made under the assumption of absent longitudinal expansion, which is justified due to the experimental constraints, as described previously.

$$\rho_{\text{VE}}(T) = \rho_{\text{IG}}(T) \cdot \left(\frac{d(T)}{d_0}\right)^2 \quad [4]$$

Furthermore, the time-dependent specific enthalpy $H(t)$ starting from room temperature can be derived by integrating the power over time and relating it to the sample mass m that is calculated from room-temperature density D_0 and diameter d_0, as well as the distance between the voltage knives l,

$$H(t) = \frac{1}{m} \cdot \int_0^t U(t') \cdot I(t') \mathrm{d}t'. \quad [5]$$

Due to the isobaric characteristics of the experiment, the specific heat capacity at constant pressure c_{p} can be evaluated from the slope of the $H(T)$ curve:

$$c_{\text{p}} = \left(\frac{\partial H}{\partial T}\right)_{\text{p}}. \quad [6]$$

In order to estimate thermal conductivity $\lambda(T)$, the Wiedemann–Franz law was used. The Lorenz number was assumed constant at the theoretical value of L = 2.45 × 10⁻⁸ V² K⁻². This assumption is justified, as the phonon conductivity of Al is reported to be very small (for more information, see Klemens and Williams.[9])

$$\lambda(T) = \frac{L \cdot T}{\rho_{\text{VE}}(T)}. \quad [7]$$

Thermal diffusivity $a(T)$ can be estimated using thermal conductivity $\lambda(T)$, specific heat capacity at constant pressure c_{p}, and density $D(T)$. Note that applying the Wiedemann–Franz law to the respective equation and inserting Eqs. [4] and [2] yields an expression independent of thermal expansion.

$$a(T) = \frac{\lambda(T)}{c_{\mathrm{p}} \cdot D(T)} \equiv \frac{L \cdot T}{c_{\mathrm{p}} \cdot \rho_{\mathrm{IG}}(T) \cdot D_0}. \qquad [8]$$

Thermal diffusivity, therefore, can be estimated with a relatively low uncertainty.[10]

B. Electromagnetic Levitation Experiments

An electromagnetic levitation (EML) setup was used to investigate the surface tension of liquid aluminum as well as to obtain additional reference data for the density of aluminum in the liquid phase. A detailed description of the EML setup was already part of precedent publications.[11–14]

In the EML experiments, small aluminum samples of high purity (99.999 at. pct) with a mass in the range of 100 to 140 mg were investigated. The samples were cut off from a high-purity aluminum rod with a diameter of 5.0 mm (Catalogue No. AL501907, Advent). Each sample was cleaned with acetone in an ultrasonic bath, followed by determining the mass on a precision balance.

A clean environment in the probe chamber was ensured by first evacuating the chamber to a pressure lower than 5×10^{-6} mbar and then flooding it close to atmospheric pressure (850 mbar) with high-purity gas mixtures of argon with 2.4 vol. pct hydrogen (AirLiquide Arcal10) and helium with 4 vol. pct hydrogen (AirLiquide custom gas mixture). The ratio of the gas mixtures was adapted throughout the experiment in order to control the heat dissipation from the sample and, thus, realize different sample temperatures. The idea of using hydrogen-enriched gas mixtures was to hinder aluminum oxide (alumina) formation and reduce already present aluminum oxide on the sample surface back to aluminum and vapor.[15]

The contactless temperature measurement was performed via a commercial NIR pyrometer (IMPAC IGA 6 Advanced, LumaSense), operating in the bandwidth of 1.45 to 1.80 μm. The temperature values recorded by the software (InfraWin 5.0.1.52) relate to the blackbody temperature (T_{bb}) of the detected radiance. In order to obtain the true temperature, the emissivity at a reference temperature was determined by assigning the recorded blackbody temperature at the solidification plateau of the sample under investigation to the real melting temperature of Al, i.e., T_{m} = 933.47 K (660.32 °C),[4] using formula [9], as given in Reference 16

$$\varepsilon = \exp\left(\frac{c_2}{\lambda} \cdot \left(\frac{1}{T_{\mathrm{m}}} - \frac{1}{T_{\mathrm{bb}}}\right)\right) \qquad [9]$$

with c_2 = 0.014388 m K, the second radiation constant. Assuming that emissivity ε does not change its value in the liquid phase over the entire temperature range, the true temperature (T_{t}) of each recorded blackbody temperature value can be recovered:[16]

$$T_{\mathrm{t}} = \left(\frac{1}{T_{\mathrm{bb}}} + \frac{\lambda}{c_2} \cdot \ln \varepsilon\right)^{-1}. \qquad [10]$$

In the EML experiment, a high-frequency current ($\approx$380 kHz) is applied to the levitation coil that generates an inhomogeneous radio frequency electromagnetic field, inducing eddy currents in the sample material. These eddy currents, according to Lenz's rule, generate an opposing electromagnetic field leading to a repulsive force that pushes the sample towards areas of lower field strength.[17]

Simultaneously, the ohmic losses of the eddy currents heat the sample to the liquid phase. Stable temperatures are obtained when heat dissipation by the atmosphere in the chamber and induced heating power are balanced.

When liquefied, oscillations of the sample around its equilibrium shape can be observed. Those variations in the radius of the sample can be described mathematically by spherical harmonics Y_l^m. Lord Rayleigh deduced a relation between the frequency of the oscillation of a spherical droplet and the surface tension (γ) that acts as the restoring force, but it is only valid under nonterrestrial conditions where the sample is force free and not rotating.[18] The fundamental frequency, called Rayleigh frequency (v_{R}), is obtained for l = 2 and is fivefold degenerated (with M being the sample's mass):

$$v_{\mathrm{R}}^2 = \frac{8 \cdot \gamma}{3 \cdot \pi \cdot M}. \qquad [11]$$

Under terrestrial conditions, those requirements are violated and the degeneracy is removed. Instead of one single oscillation frequency, up to five different oscillation modes can be observed for aspherical, rotating droplets. Cummings and Blackburn[19] derived a sum rule that recovers the original Rayleigh frequency from those five oscillation frequencies so that the surface tension can be calculated from the frequencies observed in the experiment by

$$\gamma = \frac{3}{8} \cdot \pi \cdot M \cdot \left[\frac{1}{5} \cdot \left(v_{2,0}^2 + 2 \cdot v_{2,1}^2 + 2 \cdot v_{2,2}^2\right) - v_\tau^2 \cdot \left(1.9 + 1.2 \cdot \left(\frac{z_0}{a}\right)^2\right)\right], \qquad [12]$$

$$z_0 = \frac{g}{2 \cdot (2 \cdot \pi \cdot v_\tau)^2}, \qquad [13]$$

$$a = \sqrt[3]{\frac{3 \cdot M}{4 \cdot \pi \cdot D}}, \qquad [14]$$

where z_0 is proportional to the relative position of the droplet in the field; g is the gravitational acceleration; and a is the radius of the sample, which can be calculated from the sample's mass M and density D. The term v_τ in Eqs. [12] and [13] is the mean value of the squared translation frequencies in all three spatial dimensions denoted by v_i with i = 1, 2, 3.

$$v_\tau^2 = \frac{1}{3} \cdot \sum_{i=1}^{3} v_i^2. \qquad [15]$$

The value $v_{2,0}$ in Eq. [12] is the observed frequency for the oscillation mode $l = 2$, $m = 0$. The terms $v_{2,1}$ and $v_{2,2}$ in Eq. [12] can be calculated by

$$v_{2,m} = \frac{1}{2} \cdot \left(v_{2,+m}(\Omega) + v_{2,-m}(\Omega) \right) \qquad [16]$$

since the split of the observed frequencies for the oscillation modes $l = 2$, $m = 1$, 2 due to the rotation of the sample with frequency Ω denoted by $v_{2,\pm m}(\Omega)$ is symmetrical.

The sample movement and oscillations were recorded from the top taking advantage of the vertical axis symmetry. A high-speed camera recorded 4096 images per temperature point. The framerate of the camera, typically 600 frames per second (fps) at a resolution of 1024 px · 1024 px, had to be decreased to a value as low as 200 fps for low sample temperatures to allow shutter times as high as 5 ms. This adjustment was necessary in order to ensure a sufficient brightness on the recorded images, since the spectral radiance in the visible range declined to a very low level at temperatures close to the melting point.

The image series were analyzed using an edge-detection software that detects position and size of the sample on the images. The software generates a table that holds for each image the coordinates of the center of mass as well as the radii as a function of the azimuthal angle in steps of 5 deg. Using this table, a spectrum of the coordinates as well as of the radii can be obtained by applying a fast Fourier transform to the according time series.

In order to identify the five oscillation frequencies, additional spectra of the sum and difference of two arbitrary perpendicular radii were used, as presented in Reference 13.

For the density measurement, a series of 4100 shadowgraph images acquired from the side were recorded at a framerate of 120 fps for each temperature point. From these shadowgraph images, the mean shape of the sample was determined by a software using edge detection algorithms to determine the position and size of the sample in the images.

High-precision ball bearing spheres of known diameter levitated by an argon airflow through the cooling nozzle were used to relate the area of the sample on the shadowgraph images to a real (metric) quantity. Assuming vertical axis symmetry of the droplet, the volume is calculated and, with the known sample mass, the density is determined.

III. RESULTS AND DISCUSSION

This section discusses and summarizes the new results in graphical form. It also provides the necessary polynomial coefficients to calculate the physical properties at desired temperatures (Table I). Furthermore, a collection of data values in steps of 50 K is given in Table II. The deviation of reported literature values with respect to our newly obtained values is given in parentheses within the text. Note that an aluminum

oxide layer (nanometers) will always form on the surface. The effect on temperature reduction is negligible within the investigated temperature range, however, due to the transparency of the oxide at the measuring wavelength.[20,21]

A. Density

Density was determined by means of pulse-heating and EML. In Figure 1, the results are depicted together with literature values. Extrapolating the quadratic least-squares fit describing the solid phase to the melting temperature, we obtain a density of 2514 kg m^{-3} for the onset of melting. Upon melting, the density decreases to a value of 2391 kg m^{-3}. The data obtained by averaging seven levitation experiments show a similar temperature coefficient but are shifted to lower values. However, the uncertainties of the two datasets overlap.

For comparison to other EML experiments, datasets generated from the fit coefficients reported in References 22 and 23 are depicted in Figure 1. Whereas the data of Schmitz *et al.*[23] are in good agreement with the reference data from the literature, the data of Peng *et al.*[22] show a shift to lower density values similar to our data, but the shift and its cause are not discussed. The shift of EML data to smaller density values in this publication is assumed to stem from a slight systematic overestimation of the measured sample volume caused by strong deformation oscillations or even a slight static deformation caused by the levitation coils, resulting in a violation of vertical axis symmetry. The fact that heavy samples showing larger deformations also show a bigger scatter in the density data is a strong indication for this thesis. The authors plan to extend the current experimental setup in a manner that will permit simultaneous observation of the sample from two sides in order to account for this effect by detecting deformations that violate vertical axis symmetry.[8]

The accordance of the pulse-heating data to reported literature data is promising. Assael *et al.*[24] recommend values for the liquid phase density of Al that deviate less than 0.8 pct from our data over the entire liquid phase. At the onset of melting, Mills[25] reports a density of 2558 kg m^{-3} (+1.8 pct) and 2380 kg m^{-3} after the melting transition (−0.5 pct). Touloukian[26] reports a decrease from 2542 kg m^{-3} (+1.1 pct) to 2379 kg m^{-3} (−0.5 pct) upon melting. In *Smithells Metals Reference Book*,[27] we find a value of 2385 kg m^{-3} (−0.3 pct) at the beginning of the liquid phase. Drotning[28] reports a density of 2389 kg m^{-3} (−0.1 pct) directly after melting. From specific volume data reported by Gathers,[29] the density at the beginning of the liquid phase was calculated as 2418 kg m^{-3} (+1.1 pct). His measurements were conducted at a pressure of 0.3 GPa.

B. Electrical Resistivity

Figure 2 depicts electrical resistivity as a function of temperature. Data of electrical resistivity and specific enthalpy were obtained by averaging six consecutive measurements. The dashed line represents the melting temperature, while the solid lines show the applied

Table I. Polynomial Coefficients to Describe the Results of the Present Study for Density D and Electrical Resistivity at Initial Geometry ρ_{IG}, and Corrected for Volume Expansion ρ_{VE}, Specific Enthalpy H, Thermal Conductivity λ, Thermal Diffusivity a, as well as Surface Tension γ of Al as a Function of Temperature T

| Property y | Unit | Polynomial Coefficients $y = a + bT + cT^2$ | | | Range T (K) | State |
		a	b	c		
$D(T)$	kg m^{-3}	2648	0.322	-4.99×10^{-4}	$592 \leq T \leq T_m$	s
$D(T)$	kg m^{-3}	2670	-0.299	—	$T_m \leq T \leq 1680$	l
$D^*(T)$	kg m^{-3}	2553	-0.267	—	$T_m \leq T \leq 1495$	l
$\rho_{IG}(T)$	$\mu\Omega$ m	-0.014	1.379×10^{-4}	—	$712 \leq T \leq T_m$	s
$\rho_{IG}(T)$	$\mu\Omega$ m	0.128	1.063×10^{-4}	—	$T_m \leq T \leq 1491$	l
$\rho_{VE}(T)$	$\mu\Omega$ m	-0.030	1.638×10^{-4}	—	$712 \leq T \leq T_m$	s
$\rho_{VE}(T)$	$\mu\Omega$ m	0.097	1.681×10^{-4}	—	$T_m \leq T \leq 1491$	l
$H(T)$	kJ kg^{-1}	-379	1.199	—	$712 \leq T \leq T_m$	s
$H(T)$	kJ kg^{-1}	48	1.127	—	$T_m \leq T \leq 1491$	l
$\lambda(T)$	W m^{-1} K^{-1}	248	-0.067	—	$712 \leq T \leq T_m$	s
$\lambda(T)$	W m^{-1} K^{-1}	33.9	7.892×10^{-2}	-2.099×10^{-5}	$T_m \leq T \leq 1491$	l
$a(T)$	10^{-5} m^2 s^{-1}	7.023	-9.31×10^{-4}	—	$712 \leq T \leq T_m$	s
$a(T)$	10^{-5} m^2 s^{-1}	0.965	0.31×10^{-2}	-6.306×10^{-7}	$T_m \leq T \leq 1491$	l
$\gamma^*(T)$	mN m^{-1}	993	-0.127	—	$T_m \leq T \leq 1550$	l

The terms s and l denote the solid and liquid phase, respectively. Measurements performed with EML are marked with an asterisk. The temperature range of applicability is given. T_m = 933.47 K (660.32 °C) designates the melting point.

Table II. Thermophysical Properties of Al for Different Temperatures T

T (K)	T (°C)	D (kg m^{-3})	ρ_{IG} ($\mu\Omega$ m)	ρ_{VE} ($\mu\Omega$ m)	H (kJ kg^{-1})	λ (W m^{-1} K^{-1})	a (10^{-5} m^2 s^{-1})	γ (mN m^{-1})
600	326.85	2662	—	—	—	—	—	—
650	376.85	2646	—	—	—	—	—	—
700	426.85	2629	—	—	—	—	—	—
750	476.85	2609	0.0894	0.0929	520	197.8	6.325	—
800	526.85	2586	0.0963	0.1010	580	194.4	6.278	—
850	576.85	2561	0.1032	0.1092	640	191.1	6.232	—
900	626.85	2534	0.1101	0.1174	700	187.7	6.185	—
(s)933.47	660.32	2514*	0.1147*	0.1228*	740*	185.5*	6.154*	—
(l)933.47	660.32	2391*	0.2272*	0.2539*	1100*	89.3*	3.309*	874.9*
950	676.85	2386	0.2290*	0.2567*	1119*	89.9*	3.341*	872.7*
1000	726.85	2371	0.2343*	0.2651*	1175*	91.8*	3.434*	866.3*
1050	776.85	2356	0.2396*	0.2735*	1231*	93.6*	3.525*	860.0
1100	826.85	2341	0.2449*	0.2819*	1288*	95.3*	3.612*	853.6
1150	876.85	2326	0.2502	0.2903	1344	96.9	3.696	847.3
1200	926.85	2311	0.2556	0.2987	1400	98.4	3.777	840.9
1250	976.85	2296	0.2609	0.3071	1457	99.8	3.855	834.5
1300	1026.85	2281	0.2662	0.3155	1513	101.0	3.929	828.2
1350	1076.85	2266	0.2715	0.3239	1569	102.2	4.001	821.8
1400	1126.85	2251	0.2768	0.3323	1626	103.2	4.069	815.5
1450	1176.85	2236	0.2821	0.3407	1682	104.2	4.134	809.1
1500	1226.85	2222	0.2874	0.3492	1739	105.1	4.196	802.8
1550	1276.85	2207	—	—	—	—	—	796.4
1600	1326.85	2192	—	—	—	—	—	—
1650	1376.85	2177	—	—	—	—	—	—

*Values extrapolated to the melting temperature T_m: solid state (s) and liquid state (l).

D: density obtained *via* pulse-heating, ρ_{IG}: electrical resistivity at IG, ρ_{VE}: electrical resistivity corrected for VE, H: specific enthalpy, λ: thermal conductivity, a: thermal diffusivity, and γ: surface tension.

least-squares fits. Due to the fast heating rates, the transition from the solid to the liquid phase is smeared out rather than being pronounced as expected for pure elements. The fits, therefore, were extrapolated to the melting temperature. Note that data in the solid phase must be regarded as an estimate, since the temperature

determination is based on the assumption of a non-changing emissivity in the liquid phase.

In the initial geometry, a value of ρ_{IG} = 0.1147 $\mu\Omega$ m is obtained at T_m. At the end of melting, we see a value of 0.2272 $\mu\Omega$ m. Consequently, we observe a jump in resistivity of 0.1125 $\mu\Omega$ m upon the melting process.
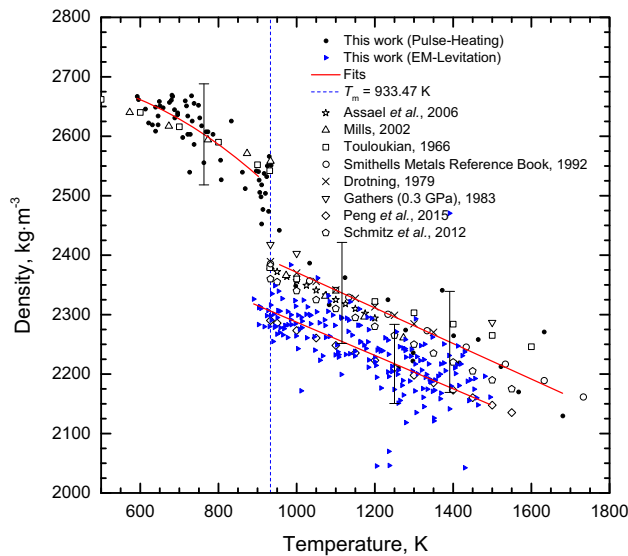
Fig. 1—Density of Al. The dashed line marks the melting tempera-ture. The solid lines represent the least-squares fits to best describe the experimental data determined in this work. Solid circles: Data obtained by pulse-heating. Solid triangles: Data obtained by EML. Diamonds: Peng et al.,[22] pentagons: Schmitz et al.,[23] stars: Assael et al.,[24] up-triangles: Mills,[25] squares: Touloukian,[26] big circles: *Smithells Metals Reference Book*,[27] crosses: Drotning,[28] and down-triangles: Gathers (0.3 GPa).[29]
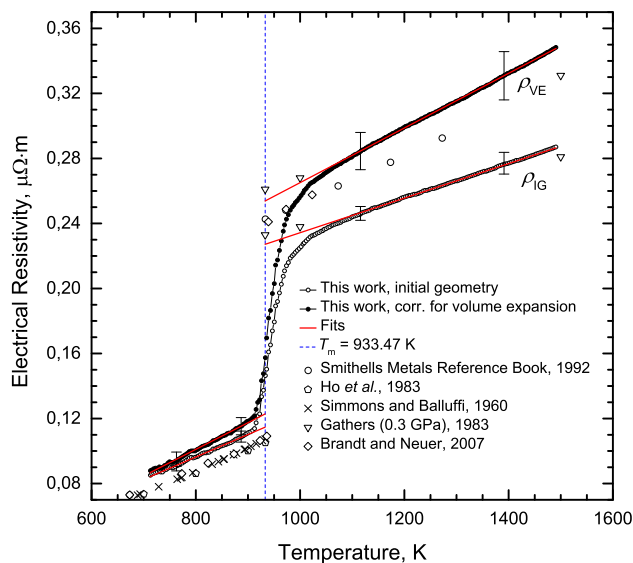
Fig. 2—Electrical resistivity of Al in initial geometry (open circles) and corrected for volume expansion (solid circles). The dashed line marks the melting point. The solid lines show the least-squares fits to the experimental data determined in this work. Diamonds: Brandt and Neuer,[32] down-triangles: Gathers, measured at 0.3 GPa,[29] big circles: *Smithells Metals Reference Book*,[27] crosses: Simmons and Balluffi,[31] and pentagons: Ho et al.[30]

The data obtained in IG were corrected using the thermal expansion data measured for density determi-nation. For the corrected electrical resistivity ρ_{VE}, values of 0.1228 and 0.2539 $\mu\Omega$ m were observed at the onset of melting and at the end of melting, respectively. This yields an increase in resistivity of 0.1311 $\mu\Omega$ m upon melting.

The recommended values reported by Ho et al.[30] were not corrected for thermal expansion. At the melting point, they report a resistivity of 0.10516 $\mu\Omega$ m (−8.3 pct). Simmons and Balluffi[31] observe a corrected value of 0.10733 $\mu\Omega$ m (−12.6 pct) at the melting point. Brandt and Neuer[32] found a corrected resistivity value of 0.1092 $\mu\Omega$ m (−11.1 pct) at the onset of melting and 0.2410 $\mu\Omega$ m (−5.1 pct) at the end of melting. This yields a jump of 0.1318 $\mu\Omega$ m upon melting, which is in excellent accordance with our newly obtained data (+0.5 pct). The data for the liquid phase reported in *Smithells Metals Reference Book*[27] were also corrected for thermal expansion. They recommend a value of 0.2425 $\mu\Omega$ m at the beginning of the liquid phase (−4.5 pct). Gathers reports liquid phase data for both the uncorrected and the corrected electrical resis-tivity.[29] These measurements were conducted under a pressure of 0.3 GPa but still show good agreement with our data. For the uncorrected and corrected resistivity, values of 0.233 $\mu\Omega$ m (+2.6 pct) and 0.261 $\mu\Omega$ m (+2.8 pct) are reported after the melting transition. The coefficients of the four least-squares fits are sum-marized in Table I, including the range of applicability.

C. Enthalpy

Specific enthalpy as a function of temperature is depicted in Figure 3, where the value at room temper-ature was chosen as zero. Upon melting, we observe a jump from 740 to 1100 kJ kg^{-1} yielding a heat of fusion of $\Delta H = 360$ kJ kg^{-1}.

A considerable amount of reference data for specific enthalpy and specific heat is present in the literature. Unfortunately, the available data are given in numerous different units, which complicates intuitive comparison. In order to keep the integrity of the discussed literature data, these values are given in their original units. However, for the sake of comparison, the literature data were additionally converted into SI units and are summarized in Table III.

Mills reports a value of 663 kJ kg^{-1} (−10.4 pct) at the beginning and 1060 kJ kg^{-1} (−3.6 pct) at the end of melting.[25] This results in a heat of fusion of $\Delta H = 397$ kJ kg^{-1} (+10.3 pct). Values reported by McDonald[33] are 4328 cal mol^{-1} (−9.3 pct) for the onset and 6888 cal mol^{-1} (−2.8 pct) at the end of melting, yielding a latent heat of $\Delta H = 2560$ cal mol^{-1} (+10.3 pct). Values of Schmidt et al.[34] show an increase from 17,430 J (g-atom)$^{-1}$ (−12.7 pct) to 28,130 J (g-atom)$^{-1}$ (−5.2 pct) upon melting. Conse-quently, they report a heat of fusion of $\Delta H = 10,700$ J (g-atom)$^{-1}$ (+10.2 pct). The recom-mended data given by Desai[35] are 18,090 J mol^{-1} (−9.4 pct) at the beginning of melting and 28,670 J mol^{-1} (−3.4 pct) at the end, yielding $\Delta H = 10,580$ J mol^{-1} (+8.9 pct). Desai states an uncertainty of 1.4 pct for his data.

Specific enthalpy data are also reported by Marchidan and Ciopec,[36] Buyco and Davis,[37] and Ditmars et al.[38] for the solid phase only. Marchidan and Ciopec report data up to a temperature of 879.26 K (606.11 °C) that are in close agreement to the literature data

discussed earlier in the text. The data of Buyco and Davis, on the other hand, 201.1 cal g^{-1} (+13.8 pct) at the beginning of melting, show a significant offset compared to the values discussed earlier, but are consistent with the value of Ditmars, i.e., 22,521 J mol^{-1} (+12.8 pct), at melting. At the beginning of the liquid phase, Gathers proposes a value of 1068 kJ kg^{-1} (+2.9 pct).[29] These measurements were conducted under a pressure of 0.3 GPa but are in close agreement to the other data reported. The fit coefficients for enthalpy vs temperature are listed in Table I.

The specific heat at constant pressure is obtained from the slope of the temperature-dependent specific enthalpy. From Table I, c_p in the liquid phase is 1.127 kJ kg^{-1} K^{-1}.

Mills[25] reports a value of c_p = 1.18 J g^{-1} K^{-1} (+4.7 pct), and McDonald reports 7.59 cal mol^{-1} K^{-1} (+4.5 pct).[33] Buyco and Davis[37] present a

recommended value of c_p = 0.2813 cal g^{-1} K^{-1} (+4.5 pct). Desai recommends a value of c_p = 31.757 J mol^{-1} K^{-1} (+4.4 pct) with an uncertainty of 3 pct.[35] The specific heat in the liquid phase proposed by Schmidt et al.[34] varies between c_p = 27.8 J (g-atom grad)$^{-1}$ (−8.6 pct) and c_p = 29.9 J (g-atom grad)$^{-1}$ (−1.7 pct) with an uncertainty of 3 pct.

D. Thermal Conductivity

In Figure 4, thermal conductivity estimated from our data using the Wiedemann–Franz law is presented as a function of temperature. The liquid phase data conform well with the reported literature data.

At the beginning of melting, we obtain a value of λ = 185.5 W m^{-1} K^{-1}. A drop in thermal conductivity is observed, resulting in 89.3 W m^{-1} K^{-1} at the end of melting.

Touloukian et al.[39] report λ = 211 W m^{-1} K^{-1} (+13.7 pct) at the onset and λ = 90.7 W m^{-1} K^{-1} (+1.6 pct) at the end of the melting process. For the solid phase, Mills[25] proposes a thermal conductivity on the basis of the Touloukian et al. values. At the beginning of the liquid phase, Mills reports a value of λ = 91 W m^{-1} K^{-1} (+1.9 pct). Smithells Metals Reference Book[27] states λ = 94.03 W m^{-1} K^{-1} (+5.3 pct) at the end of melting. Brandt and Neuer[32] calculated a value of λ = 209.6 W m^{-1} K^{-1} (+13 pct) at the end of the solid phase and λ = 95.3 W m^{-1} K^{-1} (+6.7 pct) at the beginning of the liquid phase. It can be seen from Figure 4 that their data are in close agreement to the values reported by Mills and Touloukian et al. as well as the recommended data given in Smithells Metals Reference Book for the liquid phase. Giordanengo et al.[40] report a value at the beginning of the liquid phase that is consistent with those of Smithells Metals Reference Book and Brandt and Neuer, i.e., λ = 96.2 W m^{-1} K^{-1} (+7.7 pct). The slope at the beginning of the liquid phase, however, is higher so that the deviation with respect to our data rises to 12.3 pct at a temperature of 1400 K (1127 °C).

The data of Brandt and Neuer[32] indicate that the Wiedemann–Franz law, together with the theoretically predicted Lorenz number, is indeed also applicable at
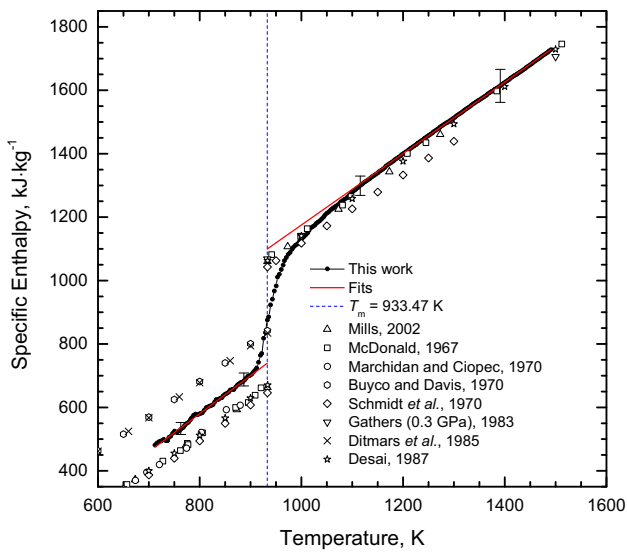

Fig. 3—Specific enthalpy of Al. The dashed line indicates the melting temperature. The solid lines mark the applied linear fits to the experimental data determined in this work (solid circles). Up-triangles: Mills,[25] squares: McDonald,[33] diamonds: Schmidt et al.,[34] stars: Desai,[35] circles: Marchidan and Ciopec,[36] hexagons: Buyco and Davis,[37] crosses: Ditmars et al.,[38] and down-triangles: Gathers, measured at 0.3 GPa.[29]

Table III. Comparison of Specific Enthalpy Values at the End of the Solid Phase $H_S(T_m)$ and at the Beginning of the Liquid Phase $H_l(T_m)$ as well as the Heat of Fusion ΔH. In addition, the Specific Heat c_p in the Liquid Phase is Given

	$H_S(T_m)$ (kJ kg^{-1})	$H_l(T_m)$ (kJ kg^{-1})	ΔH (kJ kg^{-1})	c_p (kJ kg^{-1} K^{-1})
This work	740	1100	360	1.127
Mills[25]	663	1060	397	1.18
McDonald[33]	671.5	1069	397.2	1.18
Schmidt et al.[34]	646.03	1042.6	396.6	1.03
Desai[35]	670.50	1062.6	392.1	1.1771
Buyco and Davis[37]	841.8	—	—	1.178
Ditmars et al.[38]	834.73	—	—	—
Gathers[29]	—	1068	—	—

For conversion into SI units, the factor 4.186 cal mol^{-1} and a molar weight of 26.98 g mol^{-1} were used.
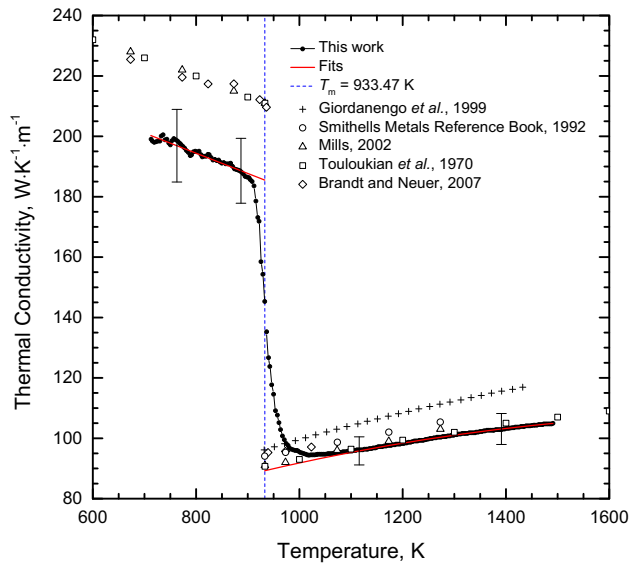
Fig. 4—Thermal conductivity of Al estimated using the Wiedemann–Franz law. The dashed line marks the melting temperature. The solid lines represent least-squares fits to the experimental data determined in this work (solid circles). Up-triangles: Mills,[25] diamonds: Brandt and Neuer,[32] circles: *Smithells Metals Reference Book*,[27] squares: Touloukian *et al.*,[39] and pluses: Giordanengo *et al.*[40]
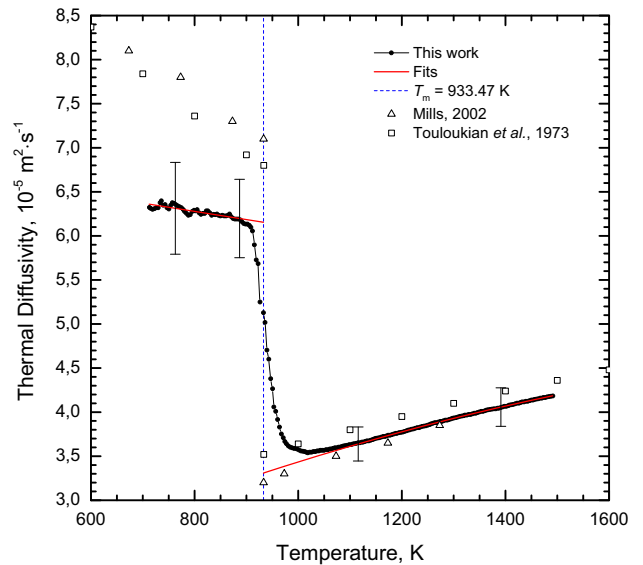

Fig. 5—Thermal diffusivity of Al. The dashed line indicates the melting temperature. The solid lines represent the least-squares fits applied to represent the data determined in this work (solid circles). Up-triangles: Mills,[25] squares: Provisional values of Touloukian *et al.*[41]

the end of the solid phase. It can be shown that our lower thermal conductivity in the solid phase is a direct result of our higher electrical resistivity applied in the Wiedemann–Franz law.

E. *Thermal Diffusivity*

By applying the Wiedemann–Franz law, thermal diffusivity can be estimated *via* the uncorrected electrical resistivity, the room-temperature density, and the specific heat derived from our $H(T)$ behavior (Figure 5). At the end of the solid phase, we report a value of $a = 6.154 \ 10^{-5} \ \mathrm{m^2 \ s^{-1}}$. Upon melting, thermal diffusivity decreases. At the end of the melting transition, we obtain a value of $a = 3.309 \ 10^{-5} \ \mathrm{m^2 \ s^{-1}}$.

Thermal diffusivity at the end of the solid phase reported by Mills[25] is $a = 7.1 \times 10^{-5} \ \mathrm{m^2 \ s^{-1}}$ ($+15.4$ pct). Touloukian *et al.*[41] gives a value of $a = 6.80 \times 10^{-5} \ \mathrm{m^2 \ s^{-1}}$ ($+10.5$ pct). The discrepancy in the solid phase is again caused by the discrepancy in solid phase electrical resistivity. The behavior in the liquid phase is consistent with literature data, Mills reporting $a = 3.2 \times 10^{-5} \ \mathrm{m^2 \ s^{-1}}$ (-3.3 pct) and Touloukian *et al.* giving a provisional value of $a = 3.52 \times 10^{-5} \ \mathrm{m^2 \ s^{-1}}$ ($+6.4$ pct) at the end of melting. The coefficients needed for the calculation of the newly obtained fits are summarized in Table I.

F. *Surface Tension*

Surface tension was determined by means of EML. Figure 6 depicts the results of six experiments together with reference data from literature. Due to the low radiance in the visible spectrum of aluminum at low
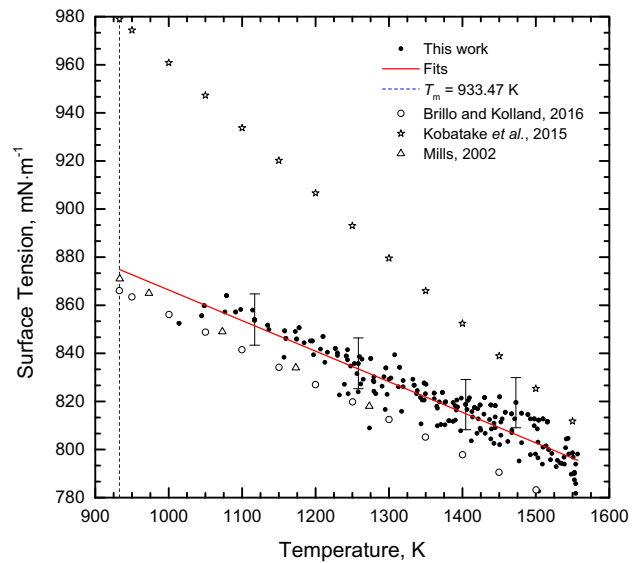

Fig. 6—Surface tension of Al. The dashed line marks the melting temperature. The solid line represents the least-squares fit to best describe the experimental data determined in this work. Solid circles: This work. Triangles: Mills,[25] stars: Kobatake *et al.*,[45] and circles: Brillo and Kolland.[44]

temperatures, data could be obtained just as close as $1014 \ \mathrm{K} \pm 21 \ \mathrm{K}$ to the melting point. The surface tension at the melting point was extrapolated from the linear fit of the data yielding a value of $875 \ \mathrm{mN \ m^{-1}}$. Datasets generated from the fit coefficients reported in 44 and 45 are added to Figure 6 or comparison with other electromagnetic levitation experiments.

Numerous publications of surface tension data of pure aluminum based on different measurement

techniques are available, but only selected publications are used here for comparison since the specification whether or not the sample material was oxygen saturated is crucial. Our samples are assumed to be oxygen saturated as the oxygen contamination of the surface is practically inevitable unless enormous effort is expended in the preparation of the experiment (*e.g.*, vacuum transfer chamber) since a nanometer-thick oxide layer[42] will form immediately after exposure of the sample to regular air.

Mills[25] data, based on a literature review by Keene,[43] have been suggested to represent oxygen saturated aluminum. The experimental data of this work are in good agreement with the reference values of Mills, who reported a surface tension of 871 mN m^{-1} (−0.5 pct) at the melting point. Our data coincide within measurement uncertainty with recent data from Brillo and Kolland.[44] Using an EML setup, they reported a surface tension of 866 mN m^{-1} (−1.0 pct) at the melting point. For the sake of completeness, data from Kobatake *et al.*[45] for pure aluminum under oxygen-reduced conditions are also depicted in Figure 6, showing a significantly higher surface tension value at the melting point of 979 mN m^{-1} (+11.9 pct) and a steeper slope for the temperature dependence.

G. *Viscosity*

Although our laboratory is not capable of measuring viscosity, for the sake of completeness, we cite the equation recommended by Assael *et al.*[24]

$$\log_{10}\left(\frac{\eta}{\eta^0}\right) = -a_1 + \frac{a_2}{T} \quad 933 \leq T(\text{K}) \leq 1270,$$

where $\eta^0 = 1$ mPa s, $a_1 = 0.7324$, and $a_2 = 803.49$ K. This equation is reported with a standard deviation of 13.7 pct at the 95 pct confidence level.

H. *Critical Point Data*

By extrapolating the liquid density data obtained by pulse-heating, the critical temperature T_c and the critical density ρ_c were estimated according to the algorithm given in the publication of Schröer and Pottlacher,[46] implemented in MATLAB R2016a.

$$T_c = \left(4.5 \, {}^{+1.1}_{-0.7}\right) \times 10^3 \text{ K}$$
$$\rho_c = (0.55 \pm 0.04) \text{ g cm}^{-3}.$$

Morel *et al.*[47] estimated T_c and ρ_c with different methods. Giving a full review, they recommend a critical temperature of $T_c = (6.7 \pm 0.8) \times 10^3$ K, which is almost 50 pct higher than our estimated value. However, the estimated values reported by different authors show a broad variation, ranging from 5115 K (5388 °C) (+13.6 pct)[48] to 9502 K (9775 °C) (+111 pct).[49] Also, further reported literature values for the critical density are as low as $\rho_c = 0.28$ g cm^{-3} (−49 pct)[50] and as high as $\rho_c = 1.03$ g cm^{-3} (+87 pct).[51] The critical density values reported by Morel *et al.*[47] are 0.566 g cm^{-3} (+2.9 pct) and 0.556 g cm^{-3} (+1.1 pct), respectively, which is in close agreement to our value.

IV. UNCERTAINTIES

The uncertainties in this work were estimated according to the *Guide to the Expression of Uncertainty in Measurement*[52] and are reported with a coverage factor of $k = 2$. Note that errors in the temperature determination due to the unknown behavior of the emissivity cannot be considered. The effect will be notable, in particular, in the solid phase, while in the liquid phase, the resulting error is typically very small. An elaborate investigation of the individual contributions to the uncertainty budgets for the setup at Graz, University of Technology, can be found in References 53, 8, and 54. As a detailed description would go well beyond the scope of this document, we give the overall uncertainties for the reported quantities in Table IV. The uncertainties for the critical temperature and the critical density were estimated from the uncertainty of the two coefficients of the $D(T)$ equation.

V. CONCLUSIONS

Thermophysical properties of aluminum were measured using two approaches. First, by means of ohmic pulse-heating, density, electrical resistivity, and specific enthalpy were obtained. Subsequently, thermal conductivity and thermal diffusivity were estimated from the derived data. Second, EML was used to measure the surface tension and the density in the liquid phase.

The newly obtained results, ranging about 600 K into the liquid phase, show excellent agreement with the literature data. The data are represented in the form of fit equations as well as in tabular form and provide another set of independent data for this important material.

Table IV. Relative Expanded Uncertainties ($k = 2$) for the Density D Obtained by Pulse-Heating, the Electrical Resistivity at IG ρ_{IG} and Corrected for VE ρ_{VE}, the Jump in Resistivity $\Delta\rho_{IG}$ and $\Delta\rho_{VE}$, Specific Enthalpy H, Latent Heat ΔH, Specific Heat Capacity at Constant Pressure c_p, Thermal Conductivity λ, Thermal Diffusivity a and Surface Tension γ

	D	ρ_{IG}	$\Delta\rho_{IG}$	ρ_{VE}	$\Delta\rho_{VE}$	H	ΔH	c_p	λ	a	γ
s	±3.3 pct	±3.4 pct	±5.7 pct	±4.8 pct	±8.9 pct	±3.5 pct	±12 pct	±5.3 pct	±6.1 pct	±8.2 pct	—
l	±3.8 pct	±2.4 pct		±4 pct		±3.3 pct		±4 pct	±5 pct	±5.4 pct	±1.5 pct

The terms s and l denote the solid and liquid phases.

In addition, critical temperature and critical density were estimated by extrapolating the liquid phase density to high temperatures. The so-obtained critical temperature is considerably lower than most values reported in the literature. The critical density, however, lies somewhere in the middle field in the broad range of reported values.

ACKNOWLEDGMENTS

OPEN ACCESS

REFERENCE

1. A. Schmon, K. Aziz, M. Luckabauer, and G. Pottlacher: *Int. J. Thermophys.*, 2015, vol. 7, pp. 1618–26.
2. B. Wilthan, C. Cagran, C. Brunner, and G. Pottlacher: *Thermochim. Acta*, 2004, vol. 415, pp. 47–54.
3. C. Cagran, T. Hüpf, B. Wilthan, and G. Pottlacher: *High Temp.-High Press.*, 2008, vol. 37, pp. 205–19.
4. H. Preston-Thomas: *Metrologia*, 1990, vol. 27, pp. 3–10.
5. G. Pottlacher and T. Hüpf: in *Thermal Conductivity 30/Thermal Expansion 18*, D.S. Gaal, ed., DEStech Publications, Inc., Lancaster, 2010, pp. 195–206.
6. D. R. Lide, Ed.: *CRC Handbook of Chemistry and Physics*, 85th ed., CRC Press, Boca Raton, FL, 2004–2005, pp. 12/219.
7. T. Hüpf: Ph.D. Thesis, Graz University of Technology, Graz, 2010.
8. A. Schmon: Ph.D. Thesis, Graz University of Technology, Graz, 2016.
9. P.G. Klemens and R.K. Williams: *Int. Met. Rev.*, 1986, vol. 31 (5), p. 208.
10. B. Wilthan, W. Schützenhöfer, and G. Pottlacher: *Int. J. Thermophys.*, 2015, vol. 36, pp. 2259–72.
11. K. Aziz, A. Schmon, and G. Pottlacher: *High Temp.-High Press.*, 2014, vol. 43, pp. 193–200.
12. K. Aziz, A. Schmon, and G. Pottlacher: *High Temp.-High Press.*, 2015, vol. 44, pp. 475–81.
13. K. Aziz, A. Schmon, E. Kaschnitz, J. Rattenberger, and G. Pottlacher: *Int. J. Thermophys.*, 2016, vol. 37, p. 15.
14. A. Schmon, K. Aziz, and G. Pottlacher: *Metall. Mater. Trans. A*, 2015, vol. 46A, pp. 2674–79.
15. O. Braaten, A. Kjekshus, and H. Kvande: *JOM*, 2000, vol. 52, pp. 47–53.
16. F. Henning: *Temperaturmessung*, Springer, Berlin, 1977, p. 136.
17. I. Egry, G. Lohöfer, and S. Sauerland: *Int. J. Thermophys.*, 1993, vol. 14, pp. 573–84.
18. J.W.S. Rayleigh: *Proc. R. Soc. Lond.*, 1897, vol. 29, pp. 71–97.
19. D.L. Cummings and D.A. Blackburn: *J. Fluid Mech.*, 1991, vol. 224, pp. 395–416.
20. O. Rozenbaum, D. De Sousa Meneses, Y. Auger, S. Chermanne, and P. Echegut: *Rev. Sci. Instrum.*, 1999, vol. 70 (10).
21. V.A. Petrov and A.Y. Vorobyev: *High Temp.-High Press.*, 2003–2007, vol. 35–36, pp. 677–89.
22. H.L. Peng, T. Voigtmann, G. Kolland, H. Kobatake, and J. Brillo: *Phys. Rev. B*, 2015, vol. 92 (18), p. 184201.
23. J. Schmitz, B. Hallstedt, J. Brillo, I. Egry, and M. Schick: *J. Mater. Sci.*, 2012, vol. 47, pp. 3706–12.
24. M.J. Assael, K. Kakosimos, R.M. Banish, J. Brillo, I. Egry, R. Brooks, P.N. Quested, K.C. Mills, A. Nagashima, Y. Sato, and W.A. Wakeham: *J. Phys. Chem. Ref. Data*, 2006, vol. 35 (1), pp. 285–300.
25. *Recommended Values of Thermophysical Properties for Selected Commercial Alloys*, K.C. Mills, ed., Woodhead Publishing Ltd, Cambridge, United Kingdom, 2002, pp. 19–25.
26. *Recommended Values of the Thermophysical Properties of Eight Alloys, Major Constituents and Their Oxides*, Y.S. Touloukian, ed., Lafayette, IN, 1966, pp. 434–35.
27. *Smithells Metals Reference Book*, 7th ed., E.A. Brandes and G.B. Brook, eds., Butterworth-Heinemann, Oxford, United Kingdom, 1992, pp. 14/7–14/10.
28. W.D. Drotning: *High Temp. Sci.*, 1979, vol. 11, pp. 265–76.
29. G.R. Gathers: *Int. J. Thermophys.*, 1983, vol. 4 (3), pp. 209–26.
30. C.Y. Ho, M.W. Ackerman, K.Y. Wu, T.N. Havill, R.H. Bogaard, R.A. Matula, S.G. Oh, and H.M. James: *J. Phys. Chem. Ref. Data*, 1983, vol. 12 (2), p. 197.
31. R.O. Simmons and R.W. Balluffi: *Phys. Rev.*, 1960, vol. 117 (1), pp. 62–68.
32. R. Brandt and G. Neuer: *Int. J. Thermophys.*, 2007, vol. 28 (5), pp. 1429–46.
33. R.A. McDonald: *J. Chem. Eng. Data*, 1967, vol. 12 (1), pp. 115–18.
34. U. Schmidt, O. Vollmer, and R. Kohlhaas: *Z. Naturforsch.*, 1970, vol. 25a, pp. 1258–64.
35. P.D. Desai: *Int. J. Thermophys.*, 1987, vol. 8 (5), pp. 621–38.
36. D.I. Marchidan and M. Ciopec: *Rev. Roum. Chimie*, 1970, vol. 15, pp. 1005–09.
37. E.H. Buyco and F.E. Davis: *J. Chem. Eng. Data*, 1970, vol. 15 (4), pp. 518–23.
38. D.A. Ditmars, C.A. Plint, and R.C. Shukla: *Int. J. Thermophys.*, 1985, vol. 6 (5), pp. 499–515.
39. *Thermophysical Properties of Matter 1—Thermal Conductivity*, Y.S. Touloukian, R.W. Powell, C.Y. Ho, and P.G. Klemens, eds., Plenum Publishing Corporation, New York, NY, 1970, p. 9.
40. B. Giordanengo, N. Benazzi, J. Vinckel, J.G. Gasser, and L. Roubi: *J. Non-Crystalline Solids*, 1999, vols. 250–252, pp. 377–83.
41. *Thermophysical Properties of Matter 10—Thermal Diffusivity*, Y.S. Touloukian, R.W. Powell, C.Y. Ho, and M.C. Nicolaou, eds., Plenum Publishing Corporation, New York, NY, 1973, p. 2.
42. T. Campbell, R.K. Kalia, A. Nakano, P. Vashishta, S. Ogata, and S. Rodgers: *Phys. Rev. Lett.*, 1999, vol. 82, pp. 4866–69.
43. B.J. Keene: *Int. Mater. Rev.*, 1993, vol. 38, pp. 157–92.
44. J. Brillo and G. Kolland: *J. Mater. Sci.*, 2016, vol. 51, pp. 4888–4901.
45. H. Kobatake, J. Brillo, J. Schmitz, and P. Pichon: *J. Mater. Sci.*, 2015, vol. 50, pp. 3351–60.
46. W. Schröer and G. Pottlacher: *High Temp.-High Press.*, 2013, vol. 43, pp. 201–15.
47. V. Morel, A. Bultel, and B.G. Chéron: *Int. J. Thermophys.*, 2009, vol. 30, pp. 1853–63.
48. S. Blairs and M.H. Abassi: *J. Coll. Interface Sci.*, 2006, vol. 304, pp. 549–53.
49. C. Boissière and G. Fiorese: *Rev. Phys. Appl.*, vol. 12, p. 857.
50. A.A. Likalter: *Phys. A*, 2002, vol. 311, pp. 137–49.
51. H.D. Jones: *Phys. Rev. A*, 1973, vol. 8 (6), pp. 3215–26.
52. Evaluation of Measurement Data—Guide to the Expression of Uncertainty in Measurement, JCGM, 2008.
53. B. Wilthan: Ph.D. Thesis, Graz University of Technology, Graz, 2005, accessible via https://www.tugraz.at/institute/iep/forschung/thermophysics-and-metalphysics/phd-theses/.
54. T. Macher: Master's Thesis, Graz University of Technology, Graz, 2014, accessible via https://www.tugraz.at/institute/iep/forschung/thermophysics-and-metalphysics/master-theses/.